Journal of ELECTRONIC MATERIALS, Vol. 49, No. 1, 2020
https://doi.org/10.1007/s11664-019-07688-4

Properties of $CuGa_2$ Formed Between Liquid Ga and Cu Substrates at Room Temperature

SHIQIAN LIU,[1] STUART MCDONALD,[1] QINFEN GU,[2] SYO MATSUMURA,[3] DONGDONG QU ,[1,5] KEITH SWEATMAN,[4] TETSURO NISHIMURA,[4] and KAZUHIRO NOGITA[1]

1.—Nihon Superior Centre for the Manufacture of Electronic Materials (NS CMEM), School of Mechanical and Mining Engineering, The University of Queensland, Brisbane, QLD 4072, Australia. 2.—Powder Diffraction Beamline, The Australian Synchrotron (ANSTO), Clayton, VIC 3168, Australia. 3.—The Ultramicroscopy Research Center, Kyushu University, Motooka 744, Nishi-ku, Fukuoka 819-0395, Japan. 4.—Nihon Superior Co., Ltd, Suita City, Osaka 564-0063, Japan. 5.—e-mail: d.qu1@uq.edu.au

Ga and Ga-based alloys have received significant attention due to their potential application in the liquid state for low-temperature bonding in microelectronics. This study investigated the interfacial reactions between liquid Ga and pure Cu substrates at room temperature. The directional thermal expansion behaviour of the resulting $CuGa_2$ was analysed by synchrotron x-ray powder diffraction with supporting observations of single crystal foils in high-voltage transmission electron microscopy. The mechanical properties of $CuGa_2$ were evaluated by nano-indentation. $CuGa_2$ was found to have advantages over other intermetallics that are present in assemblies made with current generation lead-free solders, including Ag_3Sn, Cu_6Sn_5 and Cu_3Sn. In addition to enabling lower process temperatures, solder alloys that form $CuGa_2$ at the interface with Cu offer the possibility of providing more reliable connections in the very small joints that play an increasingly important role as the trend to miniaturisation of electronics continues.

Key words: Intermetallics, liquid–solid reactions, x-ray diffraction, transmission electron microscopy

INTRODUCTION

The low melting point, 29.76°C, and high boiling point, 2403°C, of Gallium[1] provide a wide temperature range in which this unique metal can be used in the liquid state. Some Ga-based alloys, such as the binary Ga-In (eutectic Ga-24.5 wt% In, melting point 15.5°C) and the ternary Ga-In-Sn alloy (eutectic Ga-21.5 wt% In-10 wt% Sn, melting point 13.2°C), extend the range to even lower temperatures.[2,3] Ga is also considered to be non-toxic and has a low vapour pressure.[4,5] Ga and Ga-based alloys that are liquid at ambient temperature have therefore received significant attention as candidates for a range of liquid metal applications.[6]

With the widespread use of Pb-free solders in microelectronics assembly, there have been ongoing efforts to identify Sn-based alloys that can enable low-temperature soldering processes.[7] Reducing thermal loads during production results in significant energy saving and also reduces the possibility of damaging temperature-sensitive components. The low melting points and the possibility of forming intermetallic compounds (IMCs) with other metals at low temperatures[8] make Ga and Ga-based alloys promising low-temperature joining materials in microelectronics.

Studies have been performed with a view to using Ga in microelectronic interconnections.[9] Ga has been studied as an alloying addition to decrease the

(Received May 6, 2019; accepted September 26, 2019; published online October 10, 2019)

melting point of solder alloys[10,11] or as a low-melting base to be mixed with high-temperature powder fillers in transient liquid phase soldering.[12,13] A few fundamental observations on the interfacial reactions between liquid Ga-based alloys and other materials have also been documented.[9] However, these observations, summarised in Fig. 1, have mainly focused on reactions at temperatures ≥ 150°C. There has been a lack of systematic research on the interactions between Ga or Ga-based alloys with commonly used substrates for low-temperature (≤ 200°C) and ultra-low-temperature (≤ 110°C) soldering, as classified by Ribas et al.[14] Information about the interfacial reactions at low temperatures between liquid Ga-based alloys and commonly used substrates is needed to further utilise Ga and Ga-based alloys in microelectronic assembly. The mechanical properties of IMCs formed at the interface can affect the reliability of the joint in service and therefore need greater characterisation.

This study investigates the interfacial reactions between Ga and Cu substrates at room temperature with reaction times from 40 to 96 h (shown in red in Fig. 1), including the interfacial microstructure, thermal expansion behaviour and mechanical properties of $CuGa_2$. The outcomes advance the current knowledge base in the broader field of metal joining and provide a basis for the commercialisation and application of Ga-based alloys.

MATERIALS AND METHODS

A series of Ga/Cu substrate couples were prepared in an Ar atmosphere in a glovebox (O_2 < 0.10 ppm, H_2O < 0.10 ppm, pressure 4.40 Mbar, 25–26°C) to prevent oxidation. The Cu plates (99.9% purity, 30 mm × 10 mm × 3 mm, 0.875 g) were prepared by cleaning with a commercial zinc-chloride-//hydrochloric-based flux to remove oxides and other contamination and then rinsed in ethanol before the fabrication of the couples. The Ga/Cu couple samples were prepared by heating Ga ingots (99.9%, 20 g) to a liquid state at around 40°C with an electric hotplate, then following the steps illustrated in Fig. 2. First, the liquid Ga alloy (1.5 g) was dropped onto each separate Cu substrate with a transfer pipette, as shown in Fig. 2a. The couples were then assembled in the glovebox in a pure Ar atmosphere and then stored in an annealing oven at 30 ± 3°C for 40 or 96 h for the interfacial reaction between the liquid Ga drop and the clean Cu substrate to proceed. Because of its tendency to undercooling,[15] the Ga remained in the liquid state during this period, as shown in Fig. 2b. During the contact, IMC formed at the interface (Fig. 2c). After this holding period, the couples were cleaned with a 10 wt% HCl dilute solution to remove unreacted Ga while leaving the IMC on the Cu substrate (Fig. 2d).

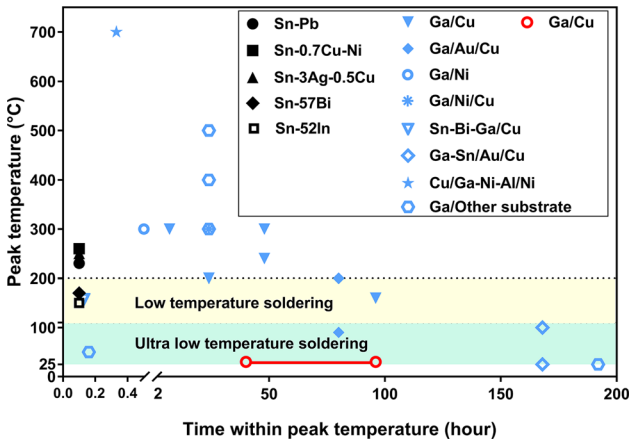

Fig. 1. Summary of the studies relating to Ga or Ga-containing alloys showing both the temperatures and times used in processing. The plot is derived from the summary tables in Ref. 9. Process conditions for conventional Sn-37Pb solders, commonly used Pb-free solders (Sn-0.7Cu-Ni and Sn-3Ag-0.5Cu), and low-temperature solders (Sn-57Bi and Sn-52In as examples) are plotted for comparison. All compositions are in wt% unless specified otherwise (Color figure online).

Microstructure Characterisation

The microstructures of the Ga-Cu IMC/Cu couples were observed both from the top view and in cross-section using scanning electron microscopy (SEM). To observe the Ga-Cu IMC/Cu reaction interface, the couples were first cold-mounted in epoxy resin and polished for metallography. SEM and energy dispersive spectroscopy (EDS) were conducted on a Hitachi TM3030 SEM. Electron

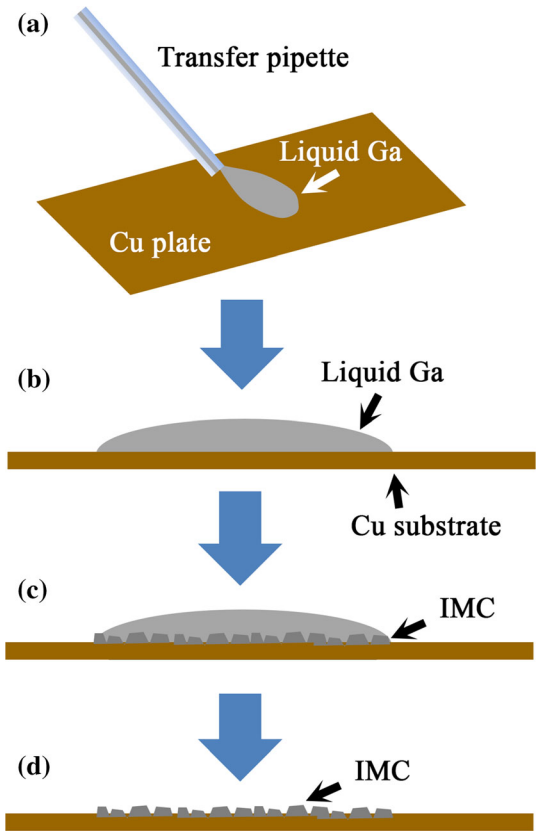

Fig. 2. Schematic of Cu-Ga IMC test couple preparation.

probe micro-analysis (EPMA) was carried out on a JEOL JXA-8200.

Powder X-ray Diffraction Measurements

In situ synchrotron x-ray diffraction (XRD) was carried out on the powder diffraction beamline at the Australian Synchrotron. The IMC on the substrates were scraped off with a sharp blade and the powders were collected and placed in a quartz capillary of 100-μm internal diameter and 10-μm wall thickness. Capillary samples were then placed on the rotary sample stage and aligned with a goniometer. Measurements were carried out 10°C intervals at ambient pressure over the temperature range from

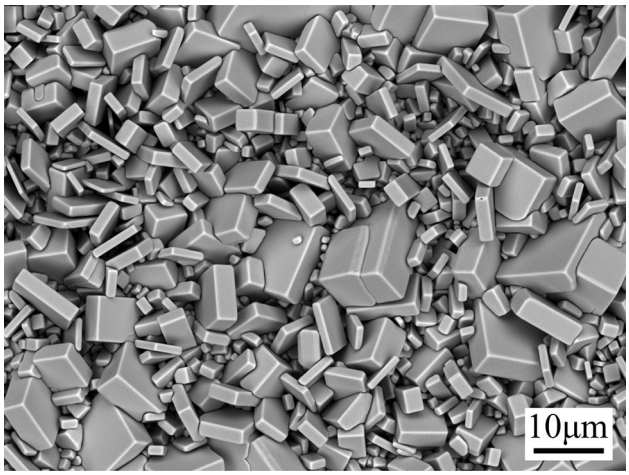

Fig. 3. SEM-backscattered electron (BSE) image of a Ga-Cu IMC on a Cu substrate (top view, reaction time 40 h).

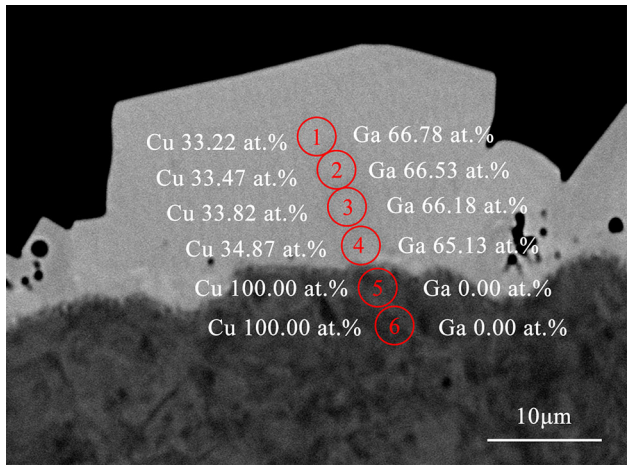

Fig. 5. Composition analysis of $CuGa_2$ by EPMA. Cu and Ga atomic concentrations (*white labels* and *numbers*) are marked along with point analysed (*red circles*) (Color figure online).

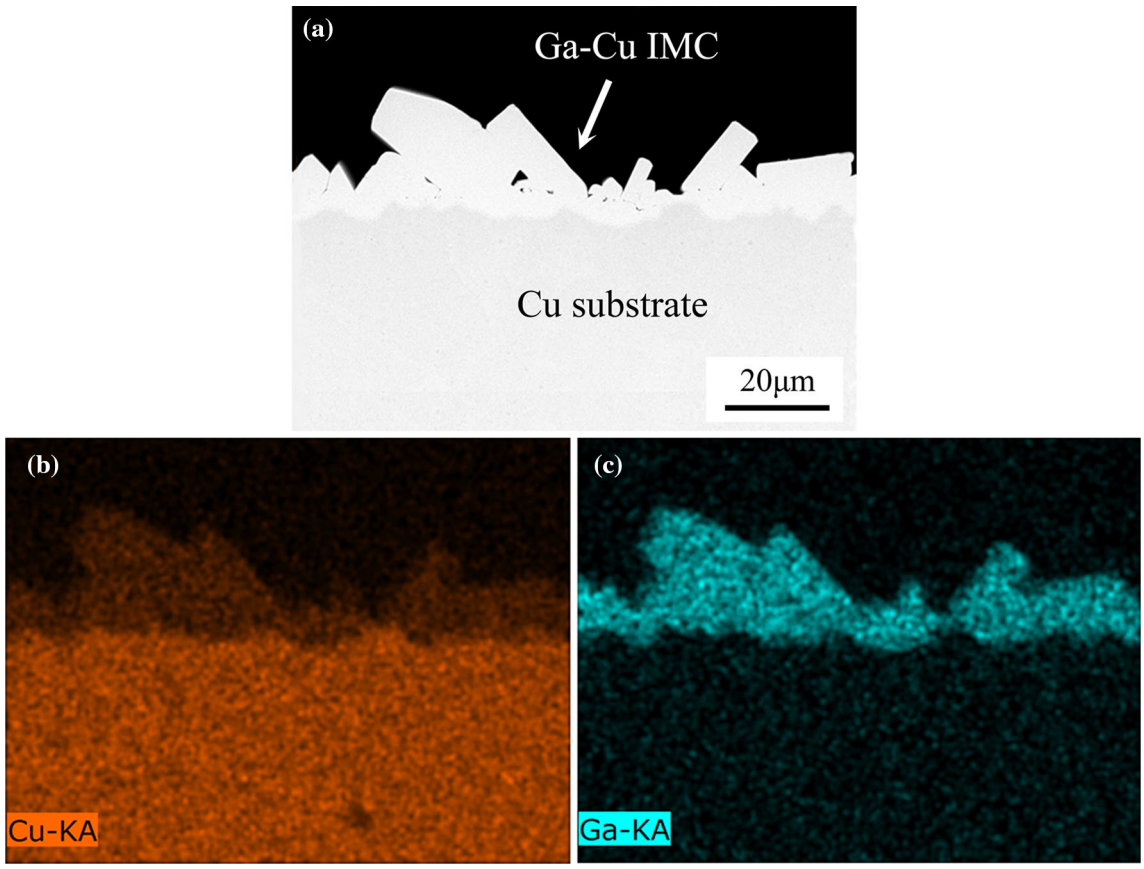

Fig. 4. SEM-BSE image (a), and EDS elemental mapping (b) and (c) of Ga-Cu IMC on a Cu substrate (cross-section, reaction time 40 h).

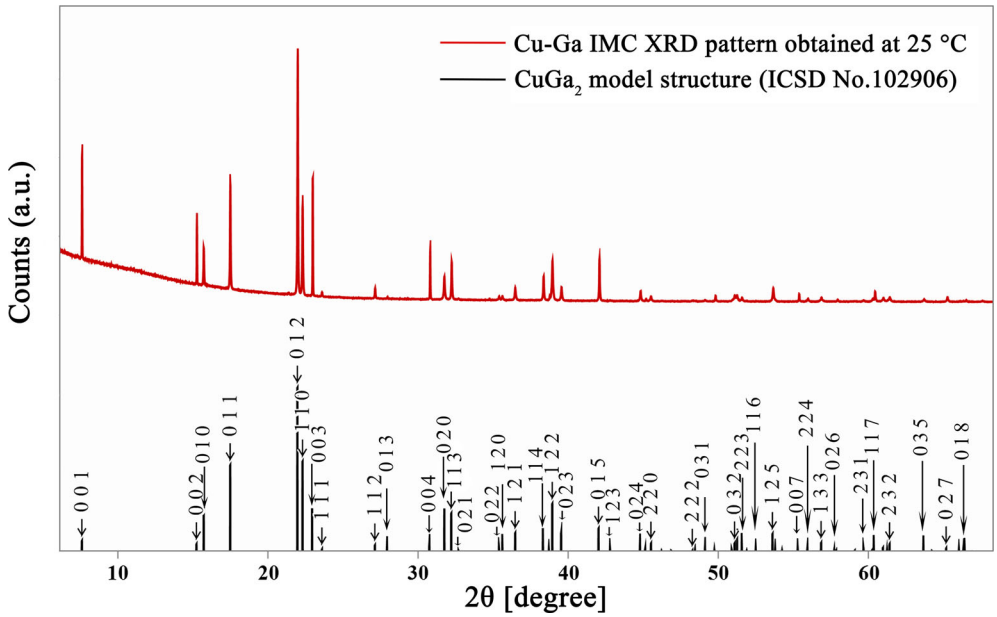

Fig. 6. Synchrotron XRD pattern indexing for $CuGa_2$ at 25°C: space group P4/mmm, Pearson symbol tP3.[17] Some peaks of the $CuGa_2$ model structure are not indexed because of the limited space in the figure.

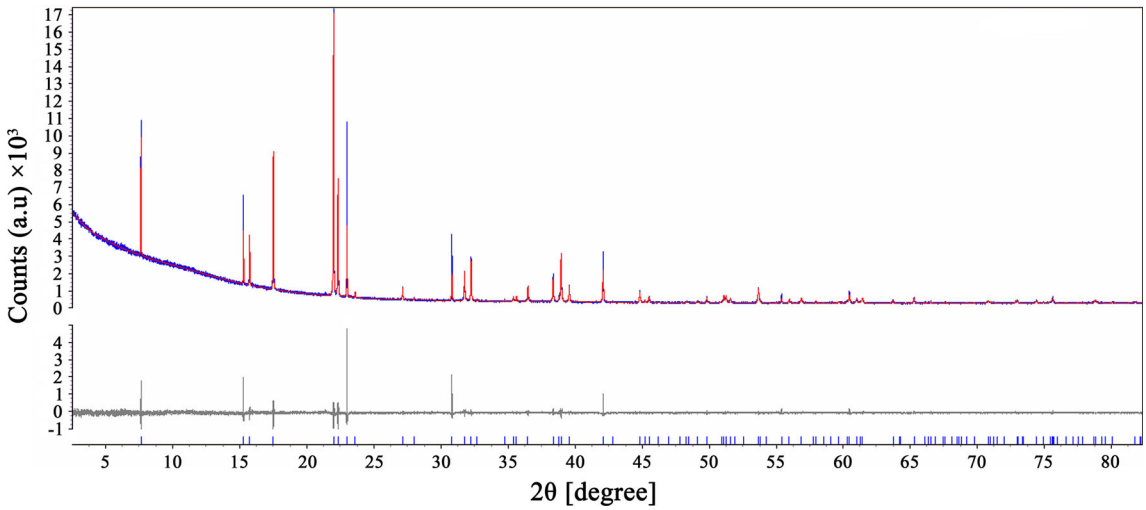

Fig. 7. Pawley refinement of the synchrotron XRD pattern for $CuGa_2$ at 25°C: space group P4/mmm, Pearson symbol tP3[17].

Table I. Crystallographic parameters, weighted-profile *R*-factor and R_{wp} obtained from the Pawely refinement of the synchrotron XRD pattern for $CuGa_2$ at 25°C

Phase	Pearson symbol	Space group	Cell parameters (Å)	*T* (°C)	Volume (Å^3)	R_{wp} (%)
$CuGa_2$	tP3	P4/mmm	a = 2.8301 c = 5.8294	25	46.764	5.785

– 100°C to 200°C with a 16-keV monochromatic incident beam. The high temperatures were achieved with a hot blower, while the low temperatures were achieved with liquid N_2 in a cryo-stage. Diffracted x-rays were recorded by a 1-D Mythen strip detector moving between two positions within 5°. The optic system for the synchrotron XRD was calibrated by measuring a standard LaB_6 sample (NIST660b, a = 4.15689 Å, $Pm\bar{3}m$, particle size 2–40 μm) in a 100-μm capillary at room temperature.

Rietveld analysis was carried out for the standard sample refinement and Pawley analysis for the

sample refinement using TOPAS 4.2 (Bruker-AXS, Germany). Phase identification of the IMC powders was carried out with the assistance of the Inorganic Crystal Structure Database. Synchrotron radiation wavelength calibration (0.7741 Å), 2θ zero error and instrument configuration functions were refined based on standard sample patterns, and were the same and fixed across all the XRD patterns. Peak shapes of the XRD patterns were described using the fundamental parameters approach, and the background, sample displacement corrections and scale factors were refined independently for each pattern. Temperature-dependent d-spacings and lattice parameters were obtained by refining the diffraction patterns.

In Situ Heating Transmission Electron Microscopy

In situ transmission electron microscopy (TEM) observations of $CuGa_2$ thermal stability in Ga alloy/Cu substrate joints during heating were carried out using high-voltage TEM (HV-TEM) equipped with an omega-type energy filter (JEM-1300NEF) at the Ultramicroscopy Research Center of Kyushu University. HV-TEM operates at much higher applied voltages (1250 kV) than conventional TEM (100–300 kV), making possible the characterization of much thicker samples than the 100 nm that is about the maximum thickness possible with conventional TEM. The high voltage in the HV-TEM also reduces inelastic beam–sample interaction as shown in the Supplementary Material (Figure S1). The calculation was carried out according to Stopping-Power and Range Tables for Electrons, Protons, and Helium of the NIST Standard Reference Database.[15] Hence, samples are less likely to be damaged by the incident electron beam under HV-TEM even when using much thicker samples.

In this study, 0.5-μm-thick joint samples for in situ HV-TEM heating observations were prepared using a FEI SCIOS focused ion beam (FIB) dual beam system. In situ heating experiments were performed from 25°C to 200°C to correlate with the synchrotron XRD analysis. TEM bright field with plasmon filter images and selected area diffraction patterns (SADPs) were taken every 10°C during heating. The actual value of the camera length was calibrated at the same accelerating voltage and objective lens setting with reference to a standard polycrystalline Au sample (a = 4.07 Å) with well-defined diffraction spacings.

Nano-indentation Hardness

Nanoindentation tests were carried out on a Triboindenter (Hysitron, Minneapolis, MN, USA) equipped with a three-sided Berkovich indenter

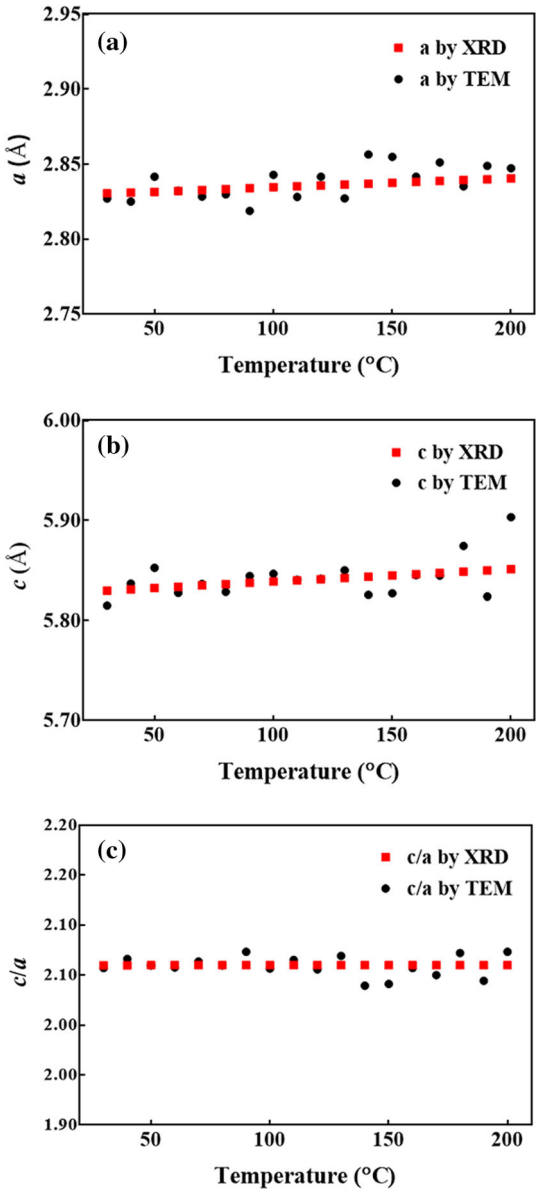

Fig. 8. $CuGa_2$ lattice parameters obtained by XRD and TEM from 25°C to 200°C: (a) cell size, *a*, (b) cell size, *c* and (c) *c/a* ratio.

with a nominal tip radius of 100 nm and a total included angle of 142.3°. Prior to testing, the indenter was calibrated using the standard sample (quartz). An indentation load of 1000 μN was applied and, during indentation, the loading, holding and unloading times were kept at 10 s, 10 s and 15 s, respectively, for all the tests. Load–displacement (P–h) curves were recorded. Morphologies of indentation impressions were characterized using in situ atomic force microscopy. Samples with relatively large IMC areas (those with reaction times of 96 h) were measured in order to obtain reliable data. Crystal orientation was determined by

electron backscattered diffraction (EBSD) on a JEOL JSM-6610 SEM.

RESULTS AND DISCUSSION

Cu-Ga IMC/Cu substrate morphology

The top view morphology of Ga-Cu IMC on the Cu plate is shown in Fig. 3. Faceted IMC grains grew on the Cu substrate after being in contact with Ga at room temperature for 40 h. Some grains were in the range of 10–20 μm long and 5–10 μm thick, while between these grains there were others smaller than 5 μm.

As the SEM image shows in Fig. 4a, the Cu substrate was covered by a continuous IMC layer, and an uneven Cu interface was found. The non-uniform morphology along the interface between the substrate and the IMC layer indicated that the Cu atoms dissolved into the liquid Ga at some sites faster than others. The "preferred dissolution sites" (for example, grain boundaries) usually have a higher defect density. Such fast dissolution along the defect interfaces may lead to the penetration of liquid Ga into the Cu substrate.

Figure 4b and c shows the EDS elemental mappings of the Ga-Cu IMC/Cu couple interface cross-section. According to the EDS point analysis results, the IMC consists of Cu and Ga with a Cu/Ga atomic ratio of 1:2, indicating that $CuGa_2$ is the most likely phase. To get more accurate elemental composition information about the IMC, EPMA was employed, as shown in Fig. 5. There was only a slight variation in the composition of the IMC from the top to the interface with the Cu substrate.

Thermal Expansion Behaviour of $CuGa_2$

Powder XRD

Figure 6 presents the indexed result of the pure Ga-Cu IMC powder synchrotron XRD pattern obtained at 25°C. The phase analysis indicated that $CuGa_2$ was the only IMC that formed between the pure Ga and Cu substrate as prepared at room temperature, which agrees well with the results of Lin et al.[16]

Figure 7 shows the full pattern Pawley refinement of $CuGa_2$ at 25°C in the 2θ range 3°–80°, where the red spectrum is the $CuGa_2$ model structure from Ref. 17 refined to fit the blue experimental spectrum. The difference plot is shown in grey. Lower blue vertical bars are aligned corresponding to different diffraction lattice planes. The accuracy of lattice parameters obtained by refinement was confirmed by the fact that refined and measured profiles vary only in the intensity of peaks but without shifts in peak positions. Table I summarises the resulting crystallographic parameters and weighted profile R-factors, R_{wp}, at 25°C. According to the information from Ref. 17, the $CuGa_2$ formed has a tetragonal crystallographic structure with the space group P4/mmm.

From a comparison of the in situ XRD patterns obtained during the heating procedure from − 100°C to 200°C, as shown in the Supplementary Material (Figure S2), $CuGa_2$ was the only phase present, and it was stable across this temperature range. The same refinement method was applied to all the XRD patterns obtained during heating. The variation of the $CuGa_2$ lattice parameters with temperature is shown in Fig. 8.

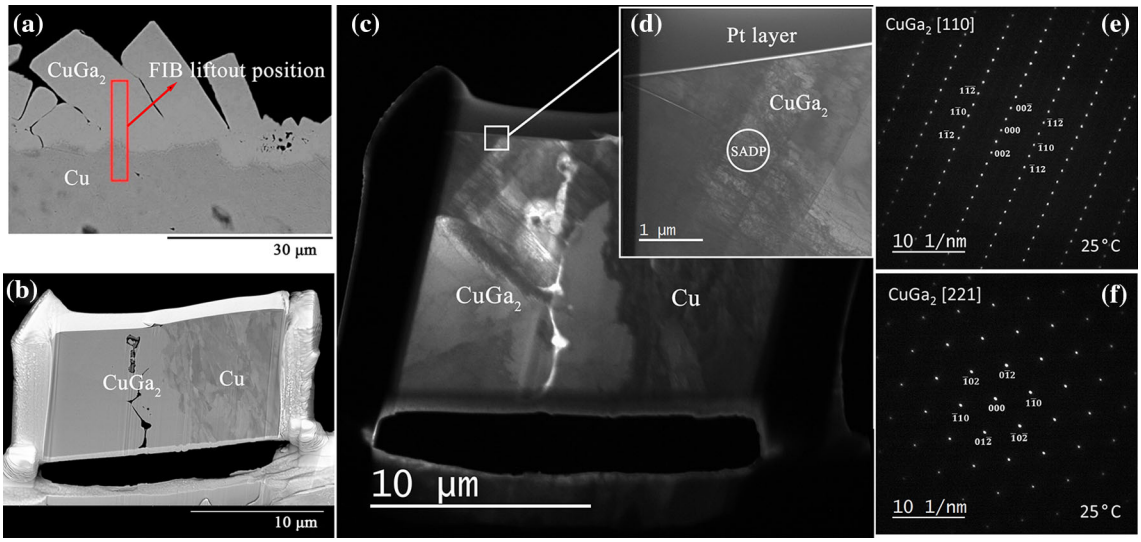

Fig. 9. (a) SEM-BSE image showing the TEM sample cut from the interface of the $CuGa_2$/Cu couple using FIB; (b) SEM-BSE image of the FIB-cut foil; (c) and (d) $CuGa_2$/Cu joint TEM plasmon-filtered bright-field images at 25°C under HV-TEM. The *white circle* in (d) indicates the region where the SADP was acquired. (e) and (f) SADPs oriented at the zone axes [110] and [221], respectively.

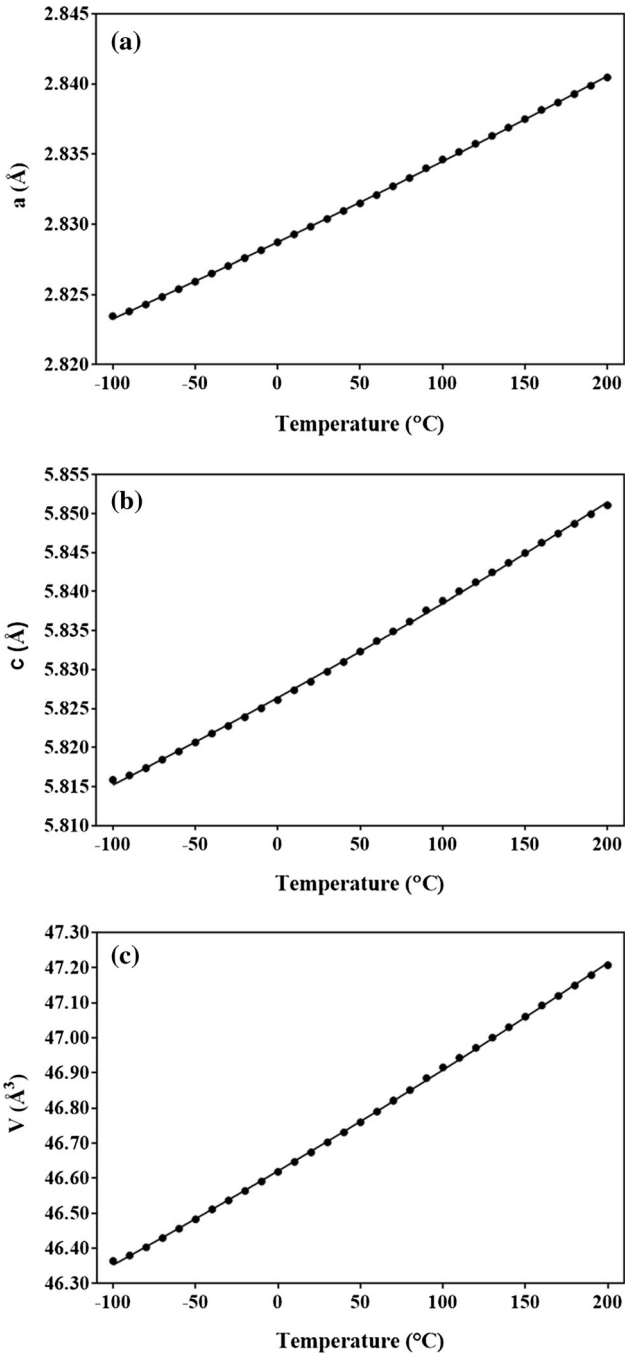

Fig. 10. $CuGa_2$ lattice parameters obtained by synchrotron XRD from − 100°C to 200°C as a function of temperature. (a) *a*; (b) *c*; (c) *V*. A second order polynomial fit is applied to each.

In Situ TEM Observation

While synchrotron XRD provided the phase identification and lattice parameters analysed from an assembly of loose IMC particles removed from the substrate, a localised observation of the Ga/Cu joint was also carried out to examine the phase stability as a function of temperature. A TEM sample from the $CuGa_2$/Cu interface was prepared by selectively cutting, as shown in Fig. 9a with FIB. The SEM image (Fig. 9b) and TEM plasmon-filtered bright-field image (Fig. 9c) of the FIB foil clearly demonstrate the $CuGa_2$, Cu substrate, as well as the interface region. Figure 9e and f demonstrates the SADPs of the Ga-Cu IMC at room temperature within different zone axes. The IMC phase was identified as the same $CuGa_2$ phase as measured by XRD. In the experimental conditions, it remained stable over the range 25–200°C. The results were consistent with the synchrotron XRD analysis and elemental identification by EDS and EPMA.

During heating from room temperature to 200°C, the joint sample was maintained in the same orientation with the zone axis [110] aligned along the incident electron beam direction. SADPs obtained every 10°C during heating were indexed. Lattice parameters of $CuGa_2$ at each measured temperature were obtained by measuring the diffraction vectors and calculating d-spacings from the same SADP. The detailed calculation is described in Supplementary Material (Figure S3 and Equations S1–S3).

As presented in Fig. 8, the lattice parameter values are relatively scattered compared to the parameters obtained by XRD. Although the values were scattered, TEM observation results showed a similar thermal expansion trend, as seen in the synchrotron XRD results. The TEM methods therefore provided supporting local information on the stability of the $CuGa_2$ phase in the real solder joint rather than independent IMC powders.

Directional CTE Determination

With the miniaturisation of solder joints, the relative proportion of the IMC layer in the total joint volume is increasing and in some cases the IMC makes up the entire joint. IMC in solder joints can play an important role in the joint reliability and influences failure mechanisms such as thermo-mechanical fatigue.[18] βSn and other IMC phases

Table II. Fitting coefficients for the temperature-dependant lattice parameters of $CuGa_2$

	C_0	C_1	C_2	R^2
a	2.829 Å	5.61×10^{-5} Å °C^{-1}	1.53×10^{-8} Å °C^{-2}	0.9999
c	5.826 Å	1.16×10^{-4} Å °C^{-1}	4.60×10^{-8} Å °C^{-2}	0.9996
V	46.620 Å^3	2.78×10^{-3} Å^3 °C^{-1}	9.32×10^{-7} Å^3 °C^{-2}	0.9998

Table III. $CuGa_2$ CTE tensor components and eigenvectors

	$A_0[10^{-6}]$	$A_1[10^{-9}]$		Direction	$A_0[10^{-6}]$	$A_1[10^{-9}]$
α_{11}	19.818	10.472	E1	[001]	19.944	15.242
α_{22}	19.818	10.472	E2	[UV0]	19.818	10.472
α_{33}	19.944	15.242	E3	[$\bar{V}$U0]	19.818	10.472
α_{12}	0	0				
α_{23}	0	0				
α_{13}	0	0				
Mean α	19.860	12.062				

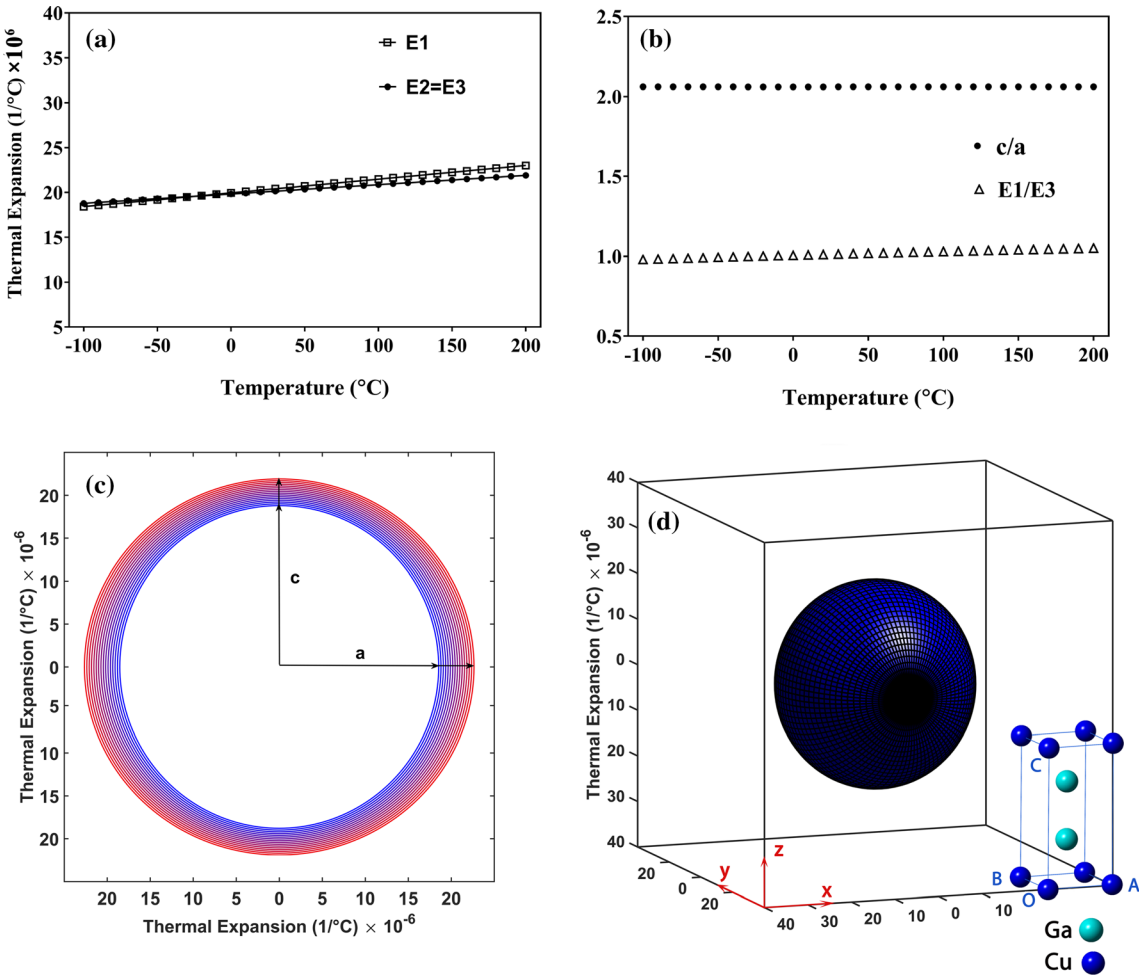

Fig. 11. (a) $CuGa_2$ CTE eigenvalues versus temperature. (b) *c/a* ratios and CTE eigenvalue E1/E3 ratios versus temperature. (c) $CuGa_2$ (010) CTE eigenvectors expansion from − 100°C to 200°C calculated by the tensor method. (d) $CuGa_2$ CTE ellipsoid at 180°C in the Cartesian coordinate system (*red axes*) relative to the tetragonal unit cell (*blue wireframe*) (Color figure online).

present in Sn-based solder joints, including Cu_6Sn_5, Ag_3Sn and Ni_3Sn_4, display an anisotropic coefficient of thermal expansion (CTE).[19,20] Differences in the thermal expansion behaviour of different phases or within a polycrystalline single phase could result in the generation of stress in thermal cycling. The directional CTE of $CuGa_2$ is therefore an important thermophysical property when considering the use of Ga-based solders in high-reliability applications.

The TEM study of $CuGa_2$ in a localized joint revealed temperature-dependent lattice parameters close to those obtained using synchrotron powder XRD. However, the scattered data points in Fig. 8 indicate a poor fit for the linear CTE calculation. For this reason, it is the XRD results, which are averaged over a large number of particles in the powder sample, that have been chosen to evaluate the thermal expansion behaviour. This XRD data

was analysed using a tensor method[19,21,22] to determine the directional CTE of $CuGa_2$.

Temperature-dependent a, c and cell volume (V) values were expressed as a second-order polynomial fit as shown in Eq. 1:

$$a\,(\text{or}\,c, V) = C_0 + C_1 T + C_2 T^2 \tag{1}$$

$CuGa_2$ lattice parameters a, c and cell volumes V are plotted as a function of temperature T in Fig. 10. The fitting coefficients C_0, C_1, C_2 and R^2 are listed in Table II for a, c and V, respectively.

Similar to the lattice sizes, a and c, the change in all d_{hkl} with $2\theta_{hkl}$ lower than 80° can also be analysed by Eq. 1. The CTE, α_{hkl}, along each hkl plane normal was then obtained by Eq. 2:

$$\alpha_{hkl} = \frac{1}{d_{hkl}} \cdot \frac{\mathrm{d}(d_{hkl})}{\mathrm{d}T} = \frac{C_1 + 2C_2 T}{C_0 + C_1 T + C_2 T^2} \tag{2}$$

On the other hand, the hkl plane can also be represented by the corresponding reciprocal space vector, $\mathbf{G_{hkl}}$ (with the same direction of the hkl plane normal, but reciprocally scaled with the hkl lattice plane spacing). Thus, CTE α_{hkl} is also responsible for the variation of $\mathbf{G_{hkl}}$ in thermal expansion. Using the coordinates transformation between reciprocal space and real space in crystallography, the variation in $\mathbf{G_{hkl}}$ can be transformed to the variation in the corresponding real space vector $[uvw]$. Then, $[uvw]$ in the crystal coordinates can be converted to the vector $[XYZ]$ in Cartesian coordinates by the following matrix:

$$\begin{bmatrix} X \\ Y \\ Z \end{bmatrix} = \begin{pmatrix} a & 0 & 0 \\ 0 & a & 0 \\ 0 & 0 & c \end{pmatrix} \cdot \begin{bmatrix} u \\ v \\ w \end{bmatrix} \tag{3}$$

For all hkl planes detected in the XRD spectrum, values of α_{hkl} along corresponding plane normals facilitate the derivation of a CTE tensor. The relationship between α_{hkl} values, $[XYZ]$ Cartesian directions (derived from hkl plane normals) and the CTE tensor $[\alpha]$ (α_{ij} components) is given by Eq. 4:[22]

$$\begin{bmatrix} \alpha_{hkl_1} \\ \vdots \\ \vdots \\ \alpha_{hkl_n} \end{bmatrix} = \begin{bmatrix} X_1^2 & Y_1^2 & Z_1^2 & X_1Y_1 & Y_1Z_1 & X_1Z_1 \\ & & & \vdots & & \\ & & & \vdots & & \\ X_n^2 & Y_n^2 & Z_n^2 & X_nY_n & Y_nZ_n & X_nZ_n \end{bmatrix} \cdot \begin{bmatrix} \alpha_{11} \\ \alpha_{22} \\ \alpha_{33} \\ 2\alpha_{12} \\ 2\alpha_{23} \\ 2\alpha_{13} \end{bmatrix} \tag{4}$$

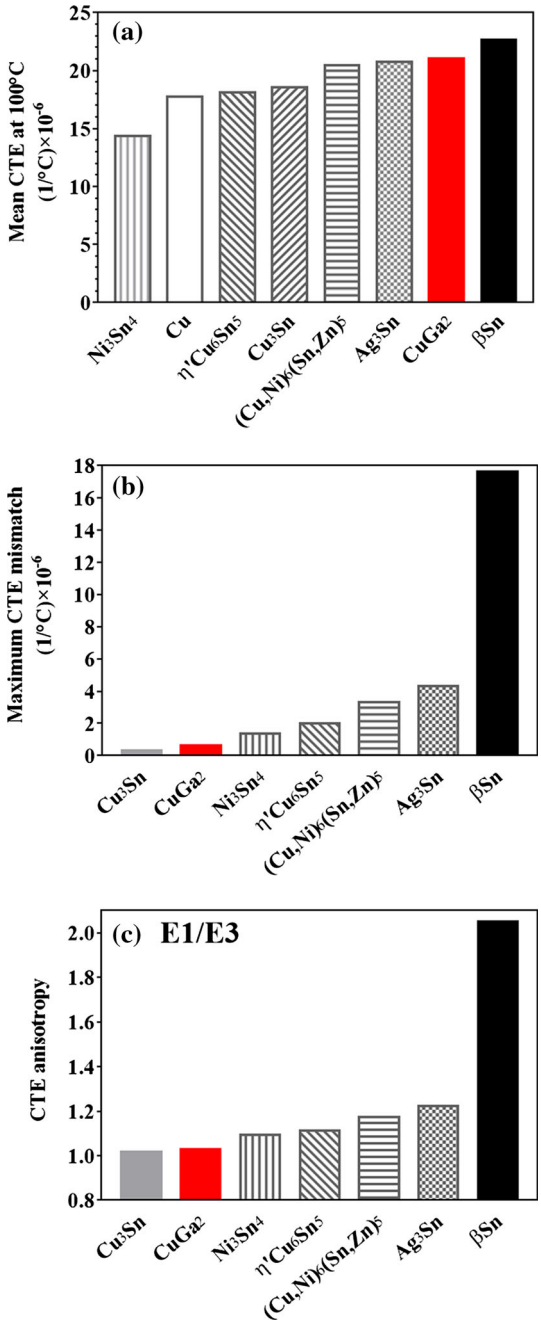

Fig. 12. (a) Mean CTE at 100°C, (b) maximum CTE mismatch and (c) CTE anisotropy of $CuGa_2$, βSn and key solder IMCs at 100°C. Data of βSn and key solder IMCs are from Ref. 19.

Note that the independent components α_{11}, α_{22} and α_{33} are along the CTE crystallographic basis vectors $\overrightarrow{OA}$, $\overrightarrow{OB}$ and $\overrightarrow{OC}$, respectively. Eigenvalues (E1, E2 and E3) and eigenvectors of the CTE tensor were then calculated from the α_{ij} components. The eigenvalues were used to plot 3D thermal expansion ellipsoids, as described in Refs. [19,21,22].

Table III shows the temperature- and orientation-dependent CTE of $CuGa_2$. The mean CTE calculated as the CTE tensor components were analysed as follows:

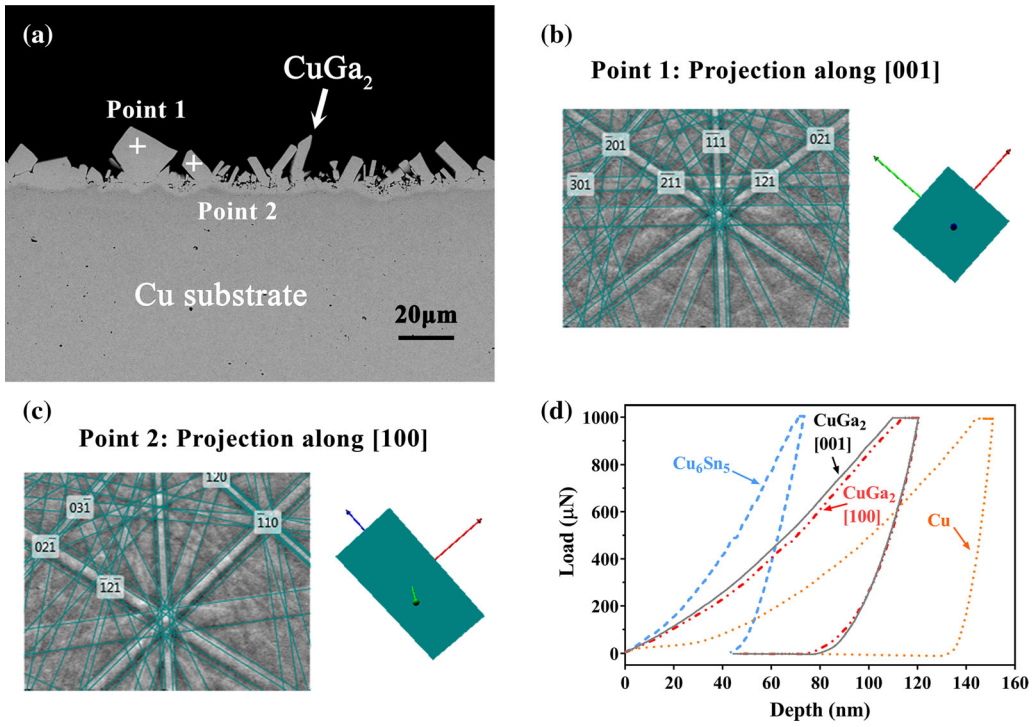

Fig. 13. (a) SEM-BSE image showing the two points for nano-indentation; EBSD Kikuchi patterns along with schematic representations for the orientations in points 1 (b) and 2 (c) in $CuGa_2$ and (d) nano-indentation load–displacement curves for pure Cu, Cu_6Sn_5 and $CuGa_2$ along zone axes [100] and [001].

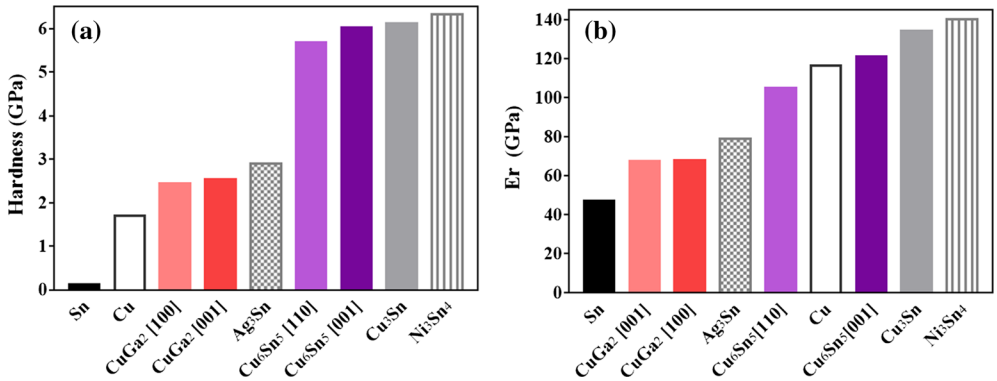

Fig. 14. Hardness (a) and Young's modulus (b) of $CuGa_2$, Cu, Sn and key solder IMCs. Data of Cu, βSn and key solder IMCs are from Ref. 28–31.

$$\alpha_{ij} = A_0 + A_1 T \tag{5}$$

where A_0 is in units of $^{\circ}C^{-1}$, A_1 is in $^{\circ}C^{-2}$ and T is in °C. The directions and modules of the eigenvectors in this tetragonal structure are listed in Table III.

Figure 11a shows the CTE eigenvalues (E1, E2 and E3) of the directional CTE as a function of temperature calculated by the tensor method with linear fits. The anisotropy of CTE can be demonstrated by calculating the temperature-dependent E1/E3 ratio and the c/a ratio as presented in Fig. 11b. While E1/E3 gradually increased from 0.9804 to 1.0504, the a/c ratio remained stable (2.0598–2.0599) over the temperature range from − 100°C to 200°C. It is clear that $CuGa_2$ expanded nearly isotropically with the CTE anisotropy increasing with temperature. In Fig. 11c, the CTE shape of $CuGa_2$ in the (010) plane from − 100°C to 200°C is visualised. The nearly isotropic property agrees well with the linear CTE reported by Zhang et al.[23]

$CuGa_2$ has a tetragonal crystal structure similar to βSn, which is known to be strongly anisotropic during thermal expansion.[24–27] In Fig. 11d, a 3D CTE ellipsoid at 180°C is plotted in a Cartesian coordinate frame with the tetragonal unit cell axes (***a***–***b***–***c***) insets. This can be understood by referring to the red axes and the blue unit cell wireframe,

where $\boldsymbol{x}$, $\boldsymbol{y}$, $\boldsymbol{z}$ is parallel to $\overrightarrow{OA}$, $\overrightarrow{OB}$ and $\overrightarrow{OC}$, respectively. Compared with the CTE ellipsoid of βSn at the same temperature with the same direction and axis limits measured by Xian et al.,[19] $CuGa_2$ shows a nearly spherical pattern instead of the "peanut" shape. This study demonstrates therefore that a tetragonal crystal structure does not necessarily mean anisotropic thermal expansion.

Comparisons among the mean CTE, CTE anisotropy (E1/E3) and maximum CTE mismatch (E1–E3) of $CuGa_2$, βSn and key IMC phases present in solder joints are shown in Fig. 12. The mean CTE value for $CuGa_2$ lies between Ag_3Sn and βSn, as shown in Fig. 12a. $CuGa_2$ is characterised by a significantly smaller anisotropy of the CTE and mismatch compared to βSn.

Young's Modulus and Hardness of $CuGa_2$

Depending on the stress distribution within the joint, the hardness of IMCs is one of the factors influencing the reliability of a solder joint in service. Nano-indentation methods were employed to characterise the hardness of $CuGa_2$ in different orientations, as shown in Fig. 13. The indentation was applied along the [001] and [100] zone axes, respectively, as shown in Fig. 13b and c.

The representative nanoindentation load–displacement curves for $CuGa_2$ and Cu_6Sn_5 are shown in Fig. 13d. The load–displacement curve for pure Cu is also included for comparison. The hardness (H) and Young's modulus (Er) are shown in Fig. 14. Compared with the other IMCs (e.g. Cu_6Sn_5, Cu_3Sn and Ni_3Sn_4) that occur in solder joints, both Young's modulus and the hardness of $CuGa_2$ are smaller, which means that $CuGa_2$ is softer and more compliant. In a solder joint, brittle IMCs are surrounded by a ductile Sn matrix. The ductile Sn matrix in a solder joint can play the role of a buffer to prevent stress concentration in brittle IMC layers. However, when IMCs make up the greater proportion of the joint volume, such as in very small solder joints that make the connections between the copper pillars of 3D integrated circuit layers, any tendency to brittleness becomes a problem. In such a situation, the greater compliance of $CuGa_2$ could provide a significant advantage. Similar to the thermal expansion property, βSn has anisotropy in the elastic properties. House and Vernon reported that the Young's modulus of Sn varied by a factor of 3 between the [100] to [001] directions.[28] The $CuGa_2$ showed less anisotropy in elastic moduli compared to βSn. In terms of elastic properties, $CuGa_2$ presents a potential advantage over the IMCs found in joints made with conventional solder alloys.

CONCLUSION

The IMC, $CuGa_2$, has been found to have a range of properties that are likely to make it more suitable, when compared to IMC particles that are present in conventional soldered joints, as the dominant IMC in very small solder joints. Ga and Ga-based alloys that form $CuGa_2$ after room-temperature reaction at interfaces with Cu are a promising alternative to conventional solder alloys that form Cu_6Sn_5 and Cu_3Sn IMCs.

The $CuGa_2$ was identified as the only IMC that forms in room temperature reactions at the interface between liquid Ga and pure Cu substrates.

In situ synchrotron XRD of $CuGa_2$ during heating from − 100°C up to 200°C combined with in situ HV-TEM from 25°C to 200°C showed consistent crystallography structural variations with temperature. $CuGa_2$ was found to be very stable from − 100°C up to 200°C. Directional CTE calculated based on XRD results showed a very small CTE anisotropy for $CuGa_2$. Nano-indentation showed a lower hardness and Young's modulus for $CuGa_2$ than Cu_6Sn_5, Cu_3Sn and Ni_3Sn_4 in joints made with conventional solder alloys. As a result, $CuGa_2$ offers potential advantages in joints where the IMC accounts for a high volume fraction.

These outcomes advance the current knowledge in the broad field of metal joining, and provide a basis for commercial application of Ga and Ga-based alloys as joining materials in electronics manufacturing.

ACKNOWLEDGMENTS

The authors are grateful for funding from the University of Queensland-Nihon Superior collaborative Research Program (Grant 2016001895), Australian Synchrotron beamtime (AS161PD10430) and the Nanotechnology Platform Project for advanced nanostructure characterization (A-17-KU-226) sponsored by MEXT, Japan. The authors acknowledge the facilities, and the scientific and technical assistance, of the Australian Microscopy and Microanalysis Research Facility at the Centre for Microscopy and Microanalysis, The University of Queensland. The authors would like to thank Dr Y.Q. Wu for his contribution to this research. S. Liu is financially supported by a University of Queensland International Scholarship and a China Scholarship Council Scholarship.

ELECTRONIC SUPPLEMENTARY MATERIAL

The online version of this article (https://doi.org/10.1007/s11664-019-07688-4) contains supplementary material, which is available to authorized users.

REFERENCES

1. W. Martienssen, *Springer Handbook of Condensed Matter and Materials,* ed. W. Martienssen and H. Warlimont (Springer, Berlin, Heidelberg, 2005), pp. 45–158.

2. M.D. Dickey, R.C. Chiechi, R.J. Larsen, E.A. Weiss, D.A. Weitz, and G.M. Whitesides, *Adv. Funct. Mater.* 18, 1097 (2008).
3. Geratherm Medical AG, Galinstan Safety Data Sheet (2011). http://www.rgmd.com/msds/msds.pdf. Accessed 22 June 2018.
4. J. Rumble, *CRC Handbook of Chemistry and Physics*, 98th ed. (Boca Raton, FL: CRC, 2017).
5. J.F. Greber, *Gallium and Gallium Compounds* (Weinheim: Wiley, 2000).
6. M.D. Dickey, *Adv. Mater.* 29, 1606425 (2017).
7. H.R. Kotadia, P.D. Howes, and S.H. Mannan, *Microelectron. Reliab.* 54, 1253 (2014).
8. Y.-G. Deng and J. Liu, *Appl. Phys. A* 95, 907 (2009).
9. S. Liu, K. Sweatman, S. McDonald, and K. Nogita, *Materials* 11, 1384 (2018).
10. C.-H. Chen, B.-H. Lee, H.-C. Chen, C.-M. Wang, and A.T. Wu, *J. Electron. Mater.* 45, 197 (2015).
11. A.A. Mikheev, V.I. Temnykh, V.S. Kazakov, E.V. Temnykh, A.E. Mityaev, G.M. Zeer, and A.K. Abkaryan, *Weld. Int.* 0, 1 (2012).
12. V.I. Temnykh, V.S. Kazakov, A.E. Mityaev, and E.V. Temnykh, *Weld. Int.* 26, 51 (2012).
13. S. Sommadossi, H.E. Troiani, and A.F. Guillermet, *J. Mater. Sci.* 42, 9707 (2007).
14. M. Ribas, H. Tom, T. Cucu, R. H V, G. Lim, and M. Murphy, The Printed Circuit Assembler's Guide to Low-Temperature Soldering, http://iconnect007.com/my-i-connect007/books/lts/. Accessed 7 Aug 2018.
15. M.J. Suplee, J.S. Coursey, M.A. Zucker, and J. Chang, ESTAR, PSTAR, and ASTAR: Computer Programs for Calculating Stopping-Power and Range Tables for Electrons, Protons, and Helium Ions (version 1.2.3) (2009). http://physics.nist.gov/Star. Accessed 7 Aug 2018.
16. S. Lin, C. Cho, and H. Chang, *J. Electron. Mater.* 43, 204 (2013).
17. M. El Boragy and K. Schubert, Kristallstruktur von CuGa2. *Z. Fur Met.* 63, 52 (1972).
18. L. Ma, Y. Zuo, S. Liu, F. Guo, and X. Wang, *J. Appl. Phys.* 113, 044904 (2013).
19. J.W. Xian, G. Zeng, S.A. Belyakov, Q. Gu, K. Nogita, and C.M. Gourlay, *Intermetallics* 91, 50 (2017).
20. T.R. Bieler, B. Zhou, L. Blair, A. Zamiri, P. Darbandi, F. Pourboghrat, T.-K. Lee, and K.-C. Liu, *J. Electron. Mater.* 41, 283 (2012).
21. R.I. Belousov and S.K. Filatov, *Glass Phys. Chem.* 33, 271 (2007).
22. Z.A. Jones, P. Sarin, R.P. Haggerty, and W.M. Kriven, *J. Appl. Crystallogr.* 46, 550 (2013).
23. Y. Zhang, J.-B. Li, J.K. Liang, Q. Zhang, B.J. Sun, Y.G. Xiao, and G.H. Rao, *J. Alloys Compd.* 438, 158 (2007).
24. G.K. White, *Phys. Lett.* 8, 294–295 (1964).
25. K. Nogita, C.M. Gourlay, S.D. McDonald, S. Suenaga, J. Read, G. Zeng, and Q.F. Gu, *Philos. Mag.* 93, 3627 (2013).
26. E.V. Vernon and S. Weintroub, *Proc. Phys. Soc. Sect. B.* 66, 887 (1953).
27. B.G. Childs, *Rev. Mod. Phys.* 25, 665 (1953).
28. D.G. House and E.V. Vernon, *Br. J. Appl. Phys.* 11, 254 (1960).
29. R.R. Chromik, R.P. Vinci, S.L. Allen, and M.R. Notis, *J. Mater. Res.* 18, 2251 (2003).
30. X. Deng, M. Koopman, N. Chawla, and K.K. Chawla, *Mater. Sci. Eng. A* 364, 240 (2004).
31. D. Mu, H. Huang, and K. Nogita, *Mater. Lett.* 86, 46 (2012).